ADVANCED FUNCTIONAL MATERIALS
www.afm-journal.de



# Controlled Incorporation of $Ni(OH)_2$ Nanoplates Into Flowerlike $MoS_2$ Nanosheets for Flexible All-Solid-State Supercapacitors

*Chunxue Hao, Fusheng Wen,* Jianyong Xiang, Limin Wang, Hang Hou, Zhibin Su, Wentao Hu, and Zhongyuan Liu**

**In this work, self-supporting three-dimensional hierarchical nanostructured $MoS_2$@$Ni(OH)_2$ nanocomposites are synthesized via a facile single-mode microwave hydrothermal technique. The fabricated $MoS_2$@$Ni(OH)_2$ nanocomposites for supercapacitors in aqueous electrolyte exhibit higher specific capacitance and better cyclic stability than those of $MoS_2$ and $Ni(OH)_2$ due to the pronounced synergistic effect between $MoS_2$ and $Ni(OH)_2$. Further, the flexible all-solid-state supercapcitor is readily constructed by composing the PVA/KOH gel electrolyte in between two $MoS_2$@$Ni(OH)_2$ electrodes on the flexible PET substrates. The resulting supercapacitors can operate at high rate up to 1000 V/s, have excellent long-life cycling stability, retaining 94.2% of the initial capacitance after 9000 cycles, and mechanical flexibility during extreme bending, respectively. Thereby, the $MoS_2$@$Ni(OH)_2$ nanocomposites are a promising electrode materials for flexible long-life cycling all-solid-sate supercapacitors.**

## 1. Introduction

The thin, lightweight and flexible all-solid-state supercapacitor (ASSP) devices have great potential applications in the fields of roll-up portable electronic devices,[1] microchips[2] and miniaturized wireless sensor networks,[3] and so forth, owing to their many advantages of rapid recharge ability, high power density, long-life cycle and environment friendly merit.[4–6] These outstanding performances depend largely on the electrochemical performance, microstructure and architecture of electrode materials.[7,8] Graphene shows advantages of large specific surface area, high in-plane electrical conductivity, and so on.[9–11] For ASSP with graphene as the electrode material, its excellent performances have been proven.[12–14] Moreover, in recent years, the layered graphene analogues of other inorganic layered materials have been attracting significant attention because of their promising applications as electrode materials.[15–17] The $VS_2$ layered nanosheets have been proven to have great potential application as ASSP electrodes.[15] The $VOPO_4$ layered nanosheets with six atomic layers is a promising material to construct a flexible ultrathin-film all-solid-state supercapacitor.[16] The $GeSe_2$ layered nanostructures have been demonstrated to be a promising candidate for design of flexible ASSP.[17] Furthermore, among layered graphene analogues, metal disulfide $MoS_2$ is one of the most potential candidates of inorganic analogues of graphene.[18,19] The layers of $MoS_2$ are formed by the covalently bonded atoms and held together by the weak van der Waals forces.[20] Recent studies have shown the excellent performances of ASSP based on $MoS_2$ films prepared by a low-cost spray painting technique and subsequent laser patterning.[21] The intensive investigation of $MoS_2$ as electrode material in ASSP further promote the layered graphene analogues applied in energy storage field.

For the layered materials, for example graphene, restacking effect of the layers leads to the significant decrease of ion-accessible surface area and thus low capacitance.[22] The restacking problem can be alleviated with insertion of conductive material, for example, carbon nanotubes, into the layers as supporting backbone.[23] On the other hand, high capacitance has been recently obtained in Faraday pseudocapacitance electrode flexible ASSP.[24] As supporting backbone, Faraday pseudocapacitance nanomaterial can play the role in prevention of restacking effect of layered graphene analogues and synergistic enhancement of energy storage performance.

In this work, we have prepared a novel kind of self-supporting three-dimensional hierarchical nanostructure $MoS_2$@$Ni(OH)_2$. In this nanostructure, Ni ions can be readily embedded onto the flowerlike $MoS_2$ nanosheets through single mode microwave-assisted hydrothermal technique (SMMHT)[25,26] for formation of $Ni(OH)_2$ nanoplates. $Ni(OH)_2$ nanoplates of pseudocapacitance materials serve as supporting backbone, and three-dimensional flowerlike $MoS_2$ nanosheets act as framework-like substrate to provide a path for ions diffusion onto the surface of pseudocapacitance materials $Ni(OH)_2$. The synergistic effect between $MoS_2$ and $Ni(OH)_2$ is not only able to effectively weaken the restacking effect of the $MoS_2$ layers, but also able to ensure the high-rate and long-life

C. Hao, Prof. F. Wen, J. Xiang, L. Wang, H. Hou, Z. Su, W. Hu, Prof. Z. Liu
State Key Laboratory of Metastable Materials Science and Technology
Yanshan University
Qinghuangdao 066004, People's Republic of China
E-mail: wenfsh03@126.com; liuzy0319@yahoo.com

DOI: 10.1002/adfm.201401268

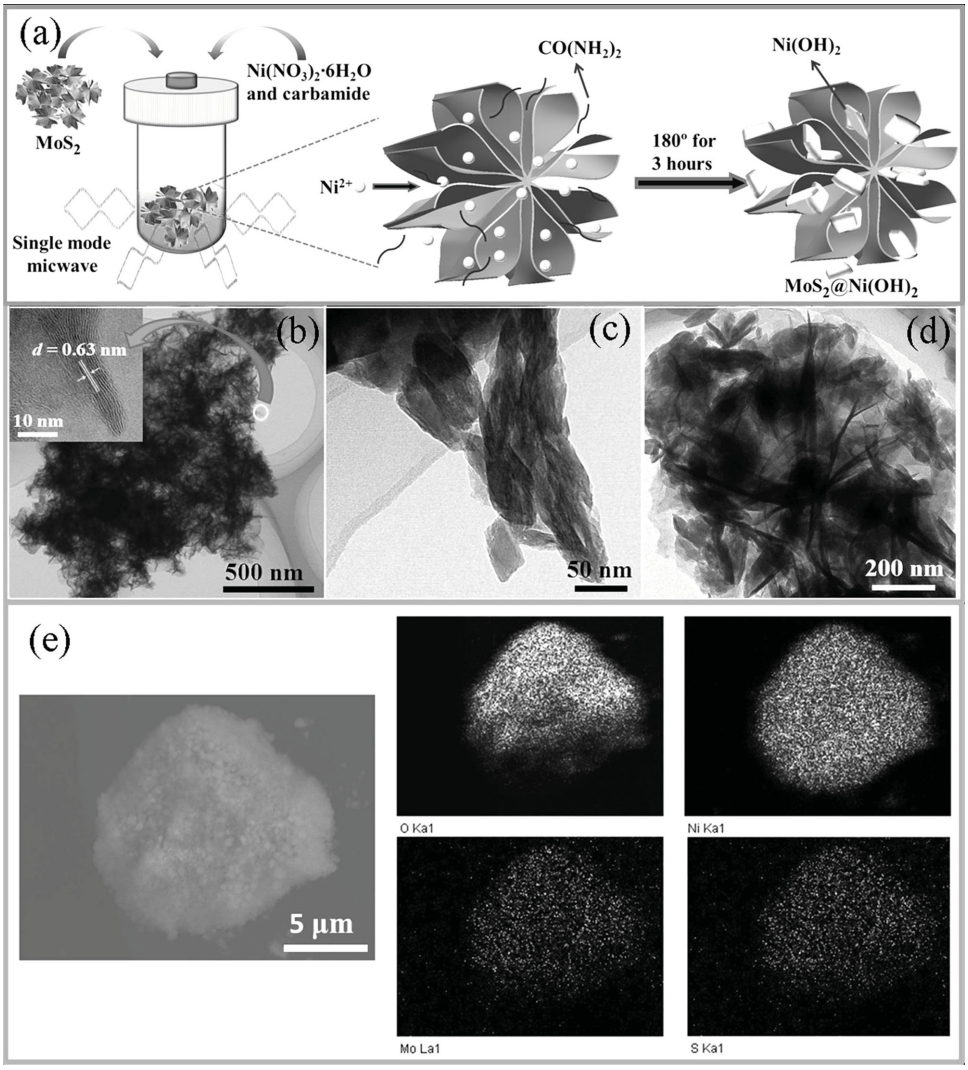


**Figure 1.** a) Schematic illustration for the formation of the self-supporting three-dimensional hierarchical nanostructure $MoS_2$@$Ni(OH)_2$ nanocomposites; TEM images of b) $MoS_2$, c) $Ni(OH)_2$, and d) $MoS_2$@$Ni(OH)_2$ nanocomposites. e) The selected area elemental mapping of $MoS_2$@$Ni(OH)_2$.

charging/discharging in the practical applications of flexible ASSP as energy storage devices.

## 2. Results and Discussion

As illustrated in **Figure 1**a, the 3D heterostructure $MoS_2$@$Ni(OH)_2$ nanocomposites were prepared by a facile two-step SMMHT-method. Firstly, the flowerlike $MoS_2$ nanosheets were fabricated through microwave irradiation in a single-mode microwave reactor. The morphology was found to depend on the reaction time (Figure S2, Supporting Information). Figures 1b gives the TEM images of the synthesized $MoS_2$ after the 12 h reaction. Clearly, interconnected nanosheets of $MoS_2$ were produced to exhibit a flowerlike shape. Inset of **Figure 2**b shows the high-resolution TEM image of a $MoS_2$ nanosheets. The observed lattice fringes indicate the good crystallinity of $MoS_2$ nanosheets. It can be seen that a well-layered structure with an interlayer distance of 0.63 nm between the (002) planes. Secondly, the flowerlike $MoS_2$ nanosheets were dispersed in a solution including $Ni(NO_3)_2{\cdot}6H_2O$ and carbamide ($CO(NH_2)_2$), and was treated at 180 °C for 3 h under SMMHT. In the absence of $MoS_2$, the microwave-assisted reaction produced the $Ni(OH)_2$ nanoplates, as revealed by the TEM images in Figures 1c. In the presence of $MoS_2$, interconnected nanosheets of $MoS_2$ serve as the substrates for the in situ growth of $Ni(OH)_2$ nanoplates. Figure 1d shows the TEM images of the finally obtained $MoS_2$@$Ni(OH)_2$ nanocomposites. The interconnected nanosheets of $MoS_2$ still keep the flowerlike shape, and serve as the substrates for growth of $Ni(OH)_2$ nanoplates. Some $Ni(OH)_2$ nanoplates embedded between the flowerlike $MoS_2$ nanosheets can be recognized. In the selected area elemental mapping of a $MoS_2$@$Ni(OH)_2$ powders as shown in Figures 1e, in addition to Mo and S, the revealed uniform distribution of Ni and O indicates the uniform attachment of $Ni(OH)_2$ nanoplates on the flowerlike $MoS_2$ nanosheets with about 10 layers.

The crystallographic structures for the samples of $MoS_2$, $Ni(OH)_2$, and $MoS_2$@$Ni(OH)_2$ nanocomposites were checked

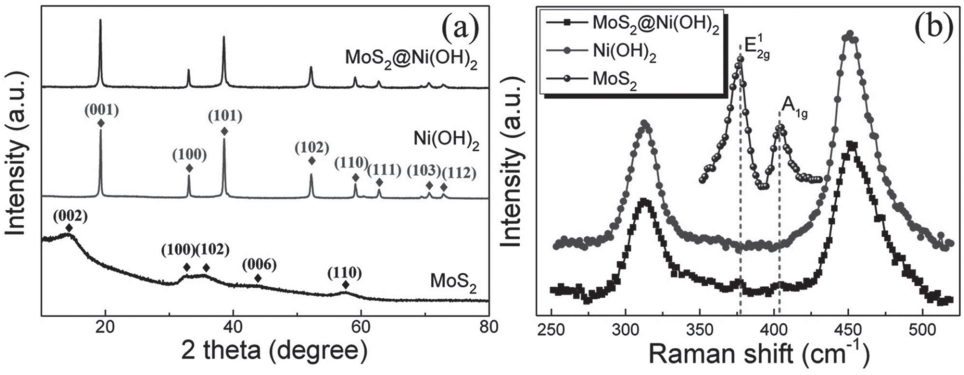


**Figure 2.** a) The XRD patterns and b) Raman spectrums for $MoS_2$, $Ni(OH)_2$ and $MoS_2$@$Ni(OH)_2$ nanocomposites.

by XRD measurements (Figure 2a). The XRD pattern of $MoS_2$ can be indexed to the hexagonal structure. The highly broadened peaks can be attributed to the small thickness of the $MoS_2$ nanosheets. In the Raman spectrum of the flowerlike $MoS_2$ nanosheets (Figure 2b), the observed Raman modes of $E^1_{2g}$ at 377.7 $cm^{-1}$ and $A_{1g}$ mode at 404.8 $cm^{-1}$ are produced by the in-plane vibration of two S atoms with opposite orientation with respect to Mo atom and the out-of-plane of S atoms, respectively.[27] It is known that the red-shift of $E^1_{2g}$ mode and blue-shift of $A_{1g}$ mode can be induced by increasing the number of $MoS_2$ layers. [28] From the Raman shift of $MoS_2$ (blue sphere), the frequency difference between the $E^1_{2g}$ and $A_{1g}$ Raman shift was determined to be ≈27.1 $cm^{-1}$, larger than the quardrilayer of $MoS_2$ (24.4 $cm^{-1}$) reported by Li [26] but similar to 10 layers (≈27 $cm^{-1}$) reported by Plechinger.[29] For the $Ni(OH)_2$ nanoplates, the reflection peaks match the standard peaks of $\beta$-$Ni(OH)_2$. In the Raman spectrum of $Ni(OH)_2$ nanoplates, the typical Raman mode peaks of $\beta$-$Ni(OH)_2$ are observed at 312 $cm^{-1}$ and 453 $cm^{-1}$, which are consistent with the results of mesoporous $\beta$-$Ni(OH)_2$.[30] For the nanostructure $MoS_2$@$Ni(OH)_2$ nanocomposites, the obtained XRD pattern is similar to that of $\beta$-$Ni(OH)_2$. In the Raman spectrum of $MoS_2$@$Ni(OH)_2$, however, the typical Raman modes of $E^1_{2g}$ and $A_{1g}$ for $MoS_2$ are clearly observed to lie between the two typical modes for $\beta$-$Ni(OH)_2$. No observation of the $MoS_2$ peaks in XRD patterns could be attributed to the ultrathin $MoS_2$ nanosheets covered with the $Ni(OH)_2$ nanoplates.

The electrochemical properties of the as-prepared $MoS_2$, $Ni(OH)_2$, and $MoS_2$@$Ni(OH)_2$ nanocomposites were separately evaluated using the typical cyclic voltammetry (CV) technique. **Figure 3**a shows the CV curves of $MoS_2$, $Ni(OH)_2$, and $MoS_2$@$Ni(OH)_2$ electrodes at a scan rate of 5 mV/s in the potential window from 0 to 0.55 V. On the CV curves of $MoS_2$ electrode, the appearance of a pair of remarkable redox peaks indicates that the flowerlike $MoS_2$ nanosheets offer more sites for redox charge transfer.[31] The average specific capacitances of the as-prepared $MoS_2$, $Ni(OH)_2$ and $MoS_2$@$Ni(OH)_2$ nanocomposites were calculated to be 228 F/g, 344 F/g and 431 F/g, respectively, at a scan rate of 5 mV/s.

Figure 3b gives the galvanostatic charging/discharging curves of $MoS_2$, $Ni(OH)_2$ and $MoS_2$@$Ni(OH)_2$ nanocomposites at a current density of 2 A/g, and the charging/discharging curves at different current densities are shown in the Figure S5a–c (Supporting Information). From the discharge curves at a discharge density of 2 A/g, the specific capacitances were calculated to be 200 and 467.3 F/g for the $MoS_2$ and $Ni(OH)_2$, which were larger than 30 F/g at 2A/g (bulk $MoS_2$, 3 M KOH)[32], and approximate to 800 F/g at 2A/g ($Ni(OH)_2$, 1 M KOH)[33] Moreover, the specific capacitances were calculated to be 516.4 F/g for the $MoS_2$@$Ni(OH)_2$ nanocomposites at a discharge density of 2 A/g. Compared to $MoS_2$ and $Ni(OH)_2$, the $MoS_2$@$Ni(OH)_2$ nanocomposites exhibit the best charge storage properties. The remarkable enhancement of the specific capacitance for $MoS_2$@$Ni(OH)_2$ nanocomposites can be mainly attributed to the architecture with synergistic effect between $MoS_2$ and $Ni(OH)_2$, in which the $MoS_2$ act not only as an active electrode material in the electrochemical reaction but also as a framework to provide more paths for insertion and extraction of ions within the $Ni(OH)_2$ edges.[34]

As shown by the gray lines in Figure 3b, the sudden drop (IR drop) in current during the discharging process is associated with the internal resistance of the electrode.[35] The IR loss values of the $MoS_2$, $Ni(OH)_2$, and $MoS_2$@$Ni(OH)_2$ electrodes are shown in Figure S5d (Supporting Information). For the nanostructure $MoS_2$@$Ni(OH)_2$ nanocomposites, the IR loss lies between those of $MoS_2$ and $Ni(OH)_2$. The discharge capacitances of these three electrodes at different current densities are plotted in Figure 3c. Significantly, the specific capacitance of $MoS_2$@$Ni(OH)_2$ nanocomposites still retain a value of as high as 244 F/g even at 10 A/g. At the same current density, the specific capacitances of $MoS_2$ and $Ni(OH)_2$ electrodes are 123.6 F/g and 147.0 F/g, respectively. Comparatively, the self-supporting three-dimensional hierarchical nanostructure $MoS_2$@$Ni(OH)_2$ with synergistic effect exhibits the best electrochemical properties. For $MoS_2$, $Ni(OH)_2$, and $MoS_2$@$Ni(OH)_2$, Figure 3d shows the capacitance retention as a function of cyclic number at the current density of 3 A/g up to 1000 cycles. It can be observed that $MoS_2$@$Ni(OH)_2$ show significantly better capacitance retention and stability than $MoS_2$ and $Ni(OH)_2$. After 1000 cycles, the specific capacitance loss is just 8% for $MoS_2$@$Ni(OH)_2$, while for the $Ni(OH)_2$ and $MoS_2$, the loss increases up to 24% and 27.3%, respectively.

As shown in **Figure 4**a, the interconnected $MoS_2$ nanosheets are found to become scattered during the electrochemical reaction and agglomerate together as large clusters after 1000 cycles. The fast fall of specific capacitance for flowerlike $MoS_2$ nanosheets after 200 cycles can be considered as the result of the aggregate and restacking effect of the layers (as shown

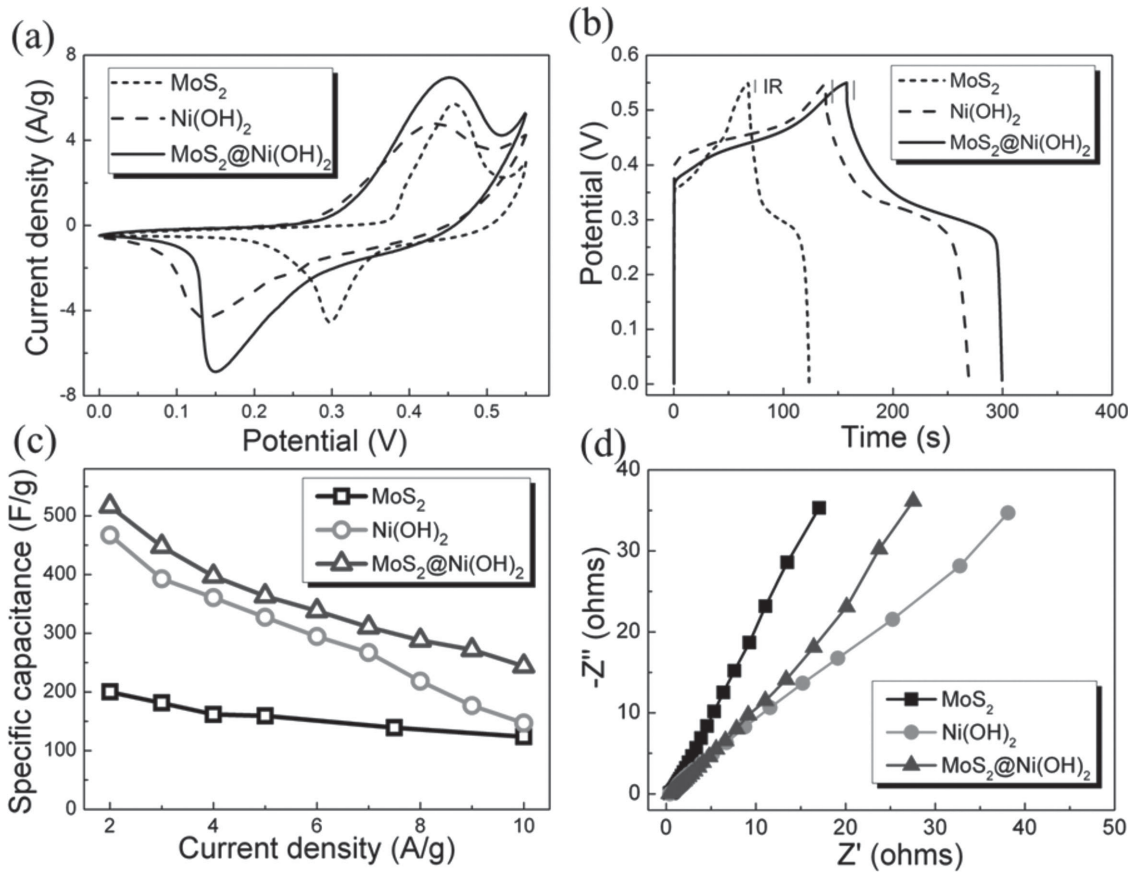


**Figure 3.** a) The cyclic voltammograms of $MoS_2$, $Ni(OH)_2$ and $MoS_2$@$Ni(OH)_2$ nanocomposites electrodes in 6 M KOH electrolyte at 5 mV/s; b) Galvanostatic charging/discharging curves of $MoS_2$,$Ni(OH)_2$ and $MoS_2$@$Ni(OH)_2$ nanocomposites electrodes at the current density of 2 A/g, the potential drop marked with the gray line is associated with the internal resistance (IR loss); c) Specific capacitance of $MoS_2$, $Ni(OH)_2$ and $MoS_2$@$Ni(OH)_2$ nanocomposites electrodes at various current densities, corresponding to the charging/discharging measurements; d) Comparison of specific capacitance retention of $MoS_2$, $Ni(OH)_2$ and $MoS_2$@$Ni(OH)_2$ nanocomposites electrodes with 1000 cycling.

in Figure 3d), which would inhibit the charge transport and active site accessibility during the cycling process. As revealed in Figure 4b, after 1000 cycles, partial framework of flowerlike $MoS_2$ nanosheets were still maintained in the presence of $Ni(OH)_2$ nanoplates. In the self-supporting three-dimensional hierarchical nanostructure, $Ni(OH)_2$ nanoplates residing in the interspace between flowerlike $MoS_2$ nanosheets act as supporting backbones to prevent the collapse of the $MoS_2$ nanosheets, while the flowerlike $MoS_2$ nanosheets serve as a framework to inhibit the aggregation of $Ni(OH)_2$ nanoplates. Thereby, the synergistic effect of $MoS_2$ nanosheets and $Ni(OH)_2$ nanoplates is able to effectively weaken the agglomerating and restacking problems during the electrochemical reaction.

By using the self-supporting three-dimensional hierarchical nanostructure $MoS_2$@$Ni(OH)_2$, flexible ASSP (MN-ASSP) device with superior properties was fabricated on a polyethylene terephthalate (PET) substrate. Firstly, small regular pieces were cut from a large PET substrate coated with a 20 nm Pt film by using dc magnetron sputtering, and then they were covered with $MoS_2$@$Ni(OH)_2$ by drop-casting. As illustrated in **Figure 5**a–e, the classical sandwich structure MN-ASSP device was assembled from these prepared pieces by gel PVA/KOH electrolyte. Figure 5f demonstrates that the sandwich-structure MN-ASSP device is flexible. The electrochemical performance of the MN-ASSP was characterized by cyclic voltammetry (CV) curves at scan rates from 0.005 to 1000 V/s (**Figure 6**). At the scan rates from 5 mV/s to 100 V/s, the obtained CV curves were close to the rectangular shape (Figure 6a–d), indicating the fast charge propagation within the electrodes. By increasing the scan rate up to 1000 V/s and above, obvious deviation from the rectangular shape is observable for the CV curves (Figure 6e,f). The area capacitance and stack capacitance were calculated from the CV curves and shown in Figure 6g. At the scan rate of 1 mV/s, 14.07 mF/cm$^2$ (in area) and 37.53 F/cm$^3$ (in volume) were achieved. By increasing the scan rate up to 1000 V/s, the capacitances of MN-ASSP device still exhibits good rate capability. The area and stack capacitances were calculated respectively to be 3.60 mF/cm$^2$ and 9.59 F/cm$^3$ at 10 mV/s, 329.80 μF/cm$^2$ and 0.88 F/cm$^3$ at 1 V/s, 28.36 μF/cm$^2$ and 75.60 mF/cm$^3$ at 100 V/s. All of these values are superior to those of the reduced graphene film sandwich-supercapacitaors.[11] Even at an ultrafast scan rate of 1,000 V/s, the MN-ASSP device still delivers an area and stack capacitance of 6.58 μF/cm$^2$ and 17.55 mF/cm$^3$. Figure 6h shows the electrochemical performance at

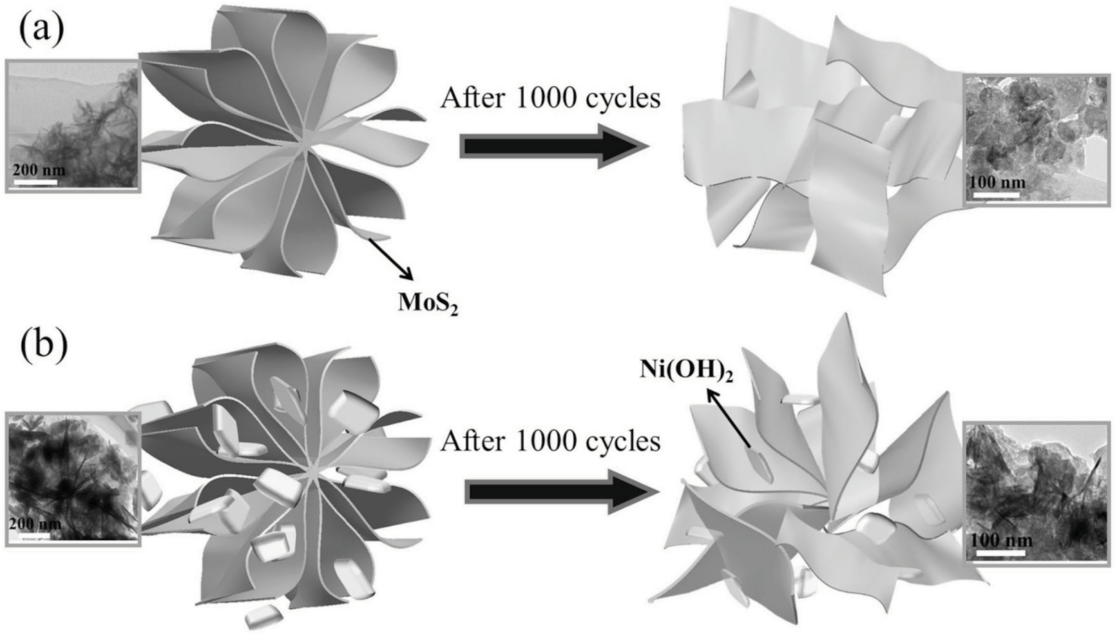


**Figure 4.** TEM images and schematics of a) $MoS_2$ and b) $MoS_2$@$Ni(OH)_2$,nanocomposites, respectively, to show the changes in morphology between the statesof pre-measurement and the 1000th cycle.

1 V/s for the MN-ASSP device with different degree of bending, which indicates the excellent flexibility and high stability of the sandwich structure device.

The cycling stability of the MN-ASSP device was examined over a large number of CV cycles at a scan rate of 1 V/s, as shown in **Figure 7**a. It is noteworthy that the capacitance retained 94.2% of the first cycling value after 9000 cycles. The excellent cycling stability could be attributed to the self-supporting synergistic effect between $MoS_2$ and $Ni(OH)_2$. The volumetric energy densities and power densities of the MN-ASSP device are compared to the previously reported values for other sandwich configuration ASSP device in Figure 7b. MN-ASSP

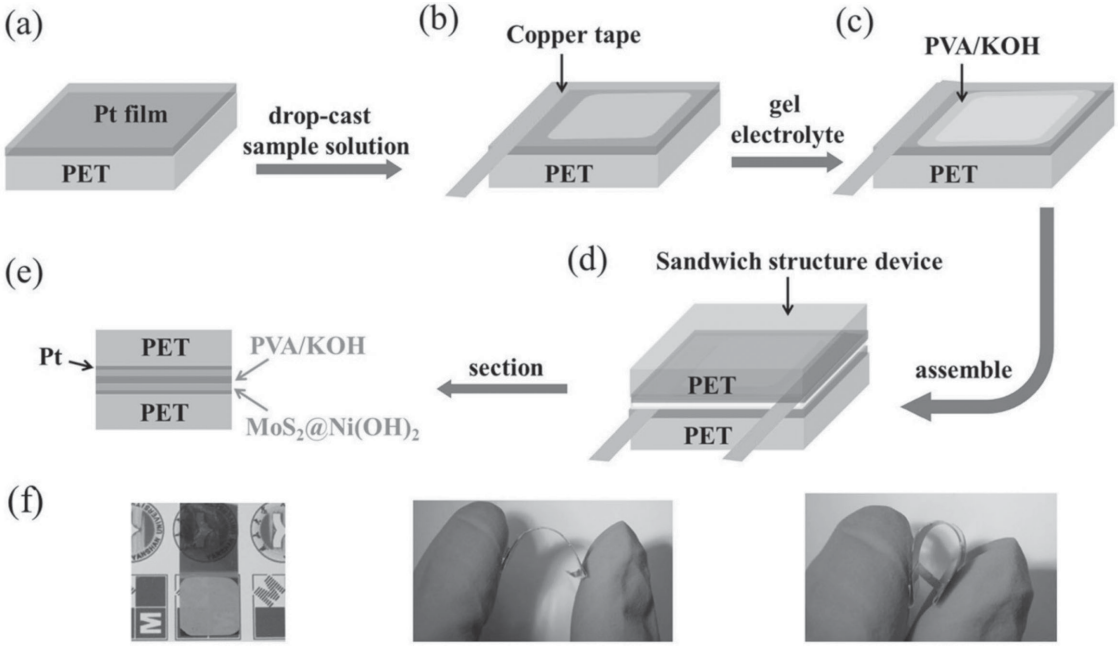


**Figure 5.** Schematic illustration of the fabrication process of a flexible MN-ASSP device. a) Growth of Pt film on PET by magnetron sputtering; b) Drop casting of $MoS_2$@$Ni(OH)_2$ solution on Pt film, and the copper tape is adhered to the edge of the device to improve the electrical contacts by silver plastic; c) Drop casting and solidification of PVA/KOH gel electrolyte; d) A sandwich structure device is assembled with two PET pieces of (c); e) Cross section of a sandwich-structure solid state supercapacitor device; f) Digital photographs of the flexible MN-ASSP.

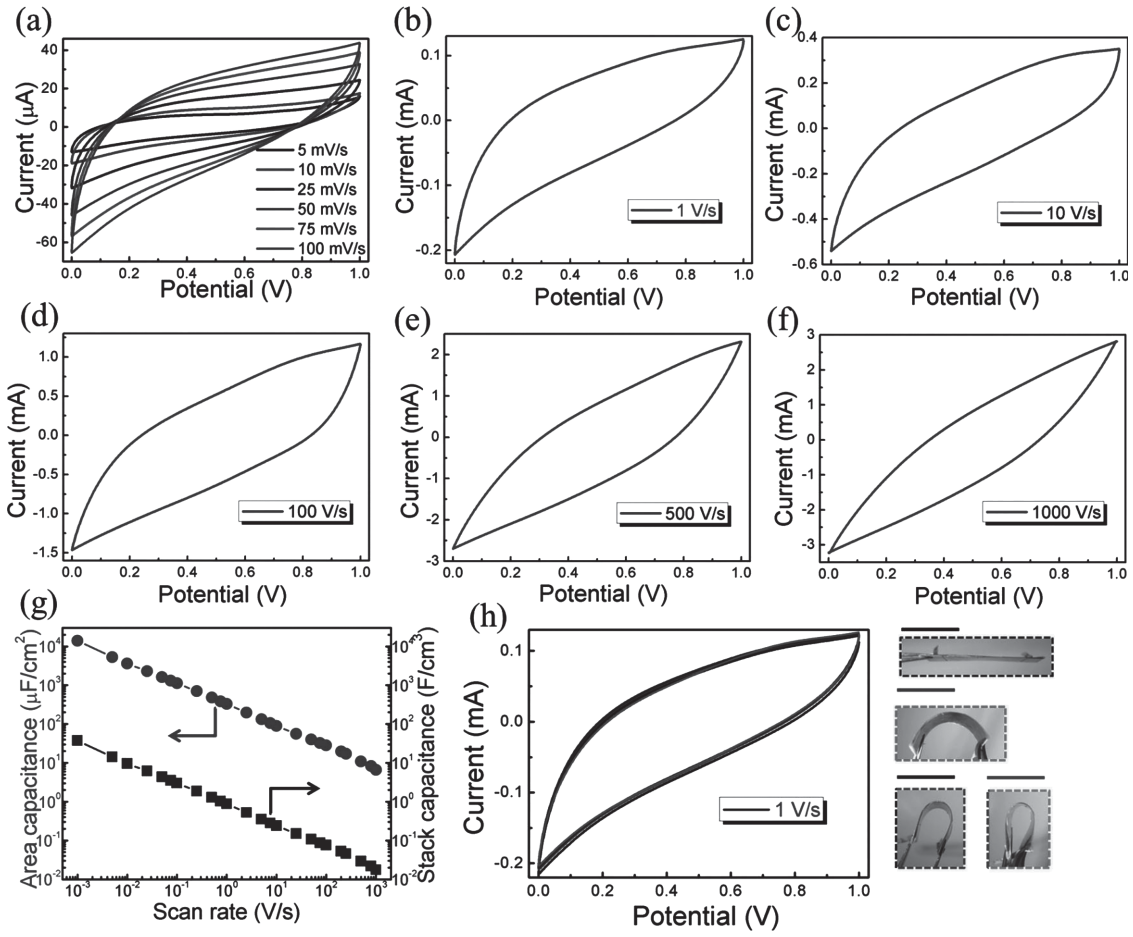


**Figure 6.** a) CV curves obtained at various scan rates from 5 mV/s to 100 mV/s in a PVA/KOH gel electrolyte on flexible PET film; b–f) CV curves at various scan rates ranging from 1 V/s to 1000 V/s; g) Area capacitance and stack capacitance of MN-ASSP device, which were calculated from the CV curves at different scan rates; h) CV curves at a scan rate of 1 V/s with different extent of bending: plat, weak bending, moderate degree of bending and strong bending.

shows a power density of 11.0 W/cm$^3$ and an energy density of 5.2 mWh/cm$^3$ in association with superior cycling stability. The MN-ASSP demonstrates energy density comparable to those of the Li-ion thin film battery, while providing about five times higher power density than Li-ion thin film battery.[12] Morever, the MN-ASSP has higher energy density than aluminium electrolytic capacitor, while providing similar power density.[12] Comparing with the state-of-the-art reduced graphene sandwich

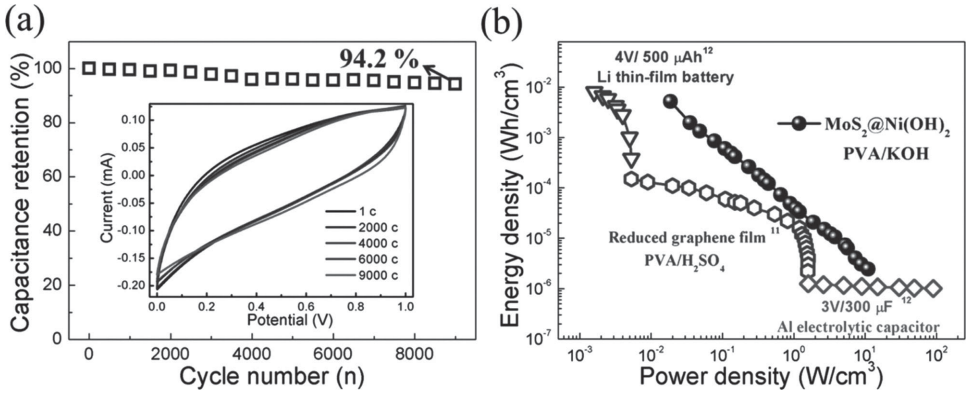


**Figure 7.** a) The cycling performance of MN-ASSP device at the scan rate of 1 V/s, insets shows the variation of CV curves with cycle numbers. b) The comparison of energy and power densities of $MoS_2$@Ni(OH)$_2$ solid-state device with Li thin-film battery, Al electrolytic capacitor and reduced graphene sandwich solid state device.

solid state device, superior energy and power performance of the MN-ASSP should compete with graphene.[11] Therefore, the remarkable cycling stability can be attributed to the self-supporting three-dimensional hierarchical nanostructure $MoS_2$@$Ni(OH)_2$ with synergistic effect. In the fabrication of flexible all-solid-state supercapacitors, the active material films are usually made not too thick, thus strongly limiting the loading mass of active materials.[11] Generally, the lower mass loading of active materials can result in the observation of higher power density. As to the observed high power density for $MoS_2$@$Ni(OH)_2$ composite in the present work, in addition to the self-supporting three-dimensional nanostructure, the role of low loading mass should not be ruled out.

## 3. Conclusions

Self-supporting three-dimensional hierarchical nanostructure $MoS_2$@$Ni(OH)_2$ nanocomposites were synthesized via a facile single-mode microwave hydrothermal technique. Compared to the separate $MoS_2$ and $Ni(OH)_2$, the $MoS_2$@$Ni(OH)_2$ nanocomposites deliver an greatly enhanced specific capacitance of 516.4 F/g at a discharge density of 2 A/g owing to the synergistic effect between $MoS_2$ and $Ni(OH)_2$. Moreover, the better cycling stability of $MoS_2$@$Ni(OH)_2$ nanocomposites can be also attributed to the self-supporting architecture. The fabricated sandwich structure MN-ASSP with $MoS_2$@$Ni(OH)_2$ nanocomposites is found to have the advantages of large capacitance (14.07 mF/cm$^2$ in area, 37.53 F/cm$^3$ in volume), excellent flexibility, high energy and power density. More significantly, the MN-ASSP device displays excellent long-time cycling stability, retaining 94.2% of the initial capacitance after 9000 cycles, respectively. These excellent electrochemical performances indicate the great potential applications of the self-supporting three-dimensional hierarchical nanostructure $MoS_2$@$Ni(OH)_2$ flexible ASSP in energy storage field for small, light-weight and flexible electronic devices.

## 4. Experimental Section

*Synthesis and Characterization of $MoS_2$, $Ni(OH)_2$ and $MoS_2$@$Ni(OH)_2$*: Three electrode materials were prepared under microwave irradiation in a single-mode microwave reactor (NOVA-II, Preekem of Shanghai, China). Typically, 15 mg sodium molybdate ($Na_2MoO_4{\cdot}2H_2O$) and 30 mg thioacetamide ($C_2H_5NS$) were dissolved into 10 mL aqueous solution with magnetic stirring, and the solution was immerged into a specialized glass tube at 180 °C for 12 h. After naturally cooling down to room temperature, the intermediate products were collected and washed with deionized water, and then dried in vacuum at 60 °C. Finally, the flowerlike $MoS_2$ nanosheets were obtained. The $Ni(OH)_2$ electrode material was synthesized by the same method. The $Ni(OH)_2$ nanoplates was produced by immerging the solution of 0.05 M $Ni(NO_3)_2{\cdot}6H_2O$ and 0.1 M carbamide (10 mL solution) into a vessel at 180 °C for 3 h. The fabrication process of $MoS_2$@$Ni(OH)_2$ nanocomposites is illustrated in Figure 1a. The prepared flowerlike $MoS_2$ nanosheets (1.2 mg) was firstly dispersed in 10 mL solution including 0.05 M $Ni(NO_3)_2{\cdot}6H_2O$ and 0.1 M carbamide ($CO(NH_2)_2$, and then put under irradiation of a single-mode microwave at 180 °C for 3 h. In the reaction process, nickel ion and carbamide could easily entry into the interspaces between the $MoS_2$ nanosheets, and their reaction leads to the formation of $Ni(OH)_2$ nanoplates on the $MoS_2$ nanosheets. Finally, the $MoS_2$@$Ni(OH)_2$ nanocomposites were collected and washed with deionized water, and dried in vacuum at 60 °C. Powder X-ray diffraction (XRD) measurements were performed with Cu-K$\alpha$ radiation ($\lambda$ = 1.5406 Å, Rigaku SmartLab in Japan). The morphologies of the samples were characterized by scanning electron microscopy (SEM, HITACH S-4800 and Phenom Pro) and transmission electron microscopy (TEM, JEM 2010). The electrochemical measurements were carried out on CHI-660E electrochemical workstation (China, Shanghai). The cyclic voltammetry (CV) and charging/discharging techniques were employed to investigate electrochemical performance of electrodes. Electrochemical impedance spectroscopy measurements were carried out in the range of 0.01 Hz to 100 kHz with ac amplitude of 5 mV.

*Electrochemical Tests of the Three-Electrode Supercapacitor System*: The electrochemical performances of $MoS_2$, $Ni(OH)_2$ and $MoS_2$@$Ni(OH)_2$ nanocomposites electrodes were measured in 6 M KOH electrolyte. The test system was a standard three-electrode configuration, including an Hg/HgO electrode as reference electrode and a platinum foil as counter electrode. As the working electrodes, the mixture containing 80 wt% electrode materials, 15 wt% acetylene black and 5 wt% polymer of vinylidene fluoride (PVDF) were agglutinated on the continuous nickel foam with a proper pressure. All the electrodes were dried under vacuum at 80 °C for 12 h prior to measurement.

*Electrochemical Tests of the All-Solid-State Supercapacitors*: The preparation of PVA/KOH electrolyte was performed as follows: 3 g PVA was dispersed into 30 mL deionized water, and then heated to 85 °C under continually stirring until clear solution was obtained. In the cooling-down process, the concentrated KOH (3.36 g) solution was dropped into the viscous solution under sufficiently stirring until a clear solution was obtained. The sandwich structure devices of $MoS_2$@$Ni(OH)_2$ were assembled in the following way: A large PET substrate was coated with 20 nm Pt film by using dc magnetron sputtering, and it was then cut into small regular pieces. These regular PET pieces were coated with the $MoS_2$@$Ni(OH)_2$ solution by drop-casting with the average thickness of 3.7 μm, and the copper tapes were adhered by silver plastic to one of their edges. The PVA/KOH electrolyte was then spread onto the $MoS_2$@$Ni(OH)_2$ electrodes. Finally, a classical sandwich structure device was obtained with two of these prepared PET pieces being pressed together and the excess water being vaporized out.

## Supporting Information

Supporting Information is available from the Wiley Online Library or from the author.

## Acknowledgements

The authors thank the National Natural Science Foundation of China (Grant No. 51271214, 51071139, 50901065, 51102206), National Science Fund for Distinguished Young Scholars (Grant No. 51025103), Program for New Century Excellent Talents in University (NCET-13–0993), Natural Science Foundation of Hebei Province (Grant No. E2014203144), Science Foundation for the Excellent Youth Scholars from Universities and Colleges of Hebei Province (YQ2014009), Research Program of the College Science & Technology of Hebei Province (QN2014047).

Received: April 20, 2014
Revised: May 30, 2014
Published online: August 28, 2014

[1] C. Z. Meng, C. G. Liu, L. Z. Chen, C. H. Hu, S. S. Fan, *Nano Lett.* **2010**, *10*, 4025.
[2] D. Pech, M. Brunet, H. Durou, P. H. Huang, V. Mochalin, Y. Gogotsi, P. L. Tabena, P. Simon, *Nat. Nanotechnol.* **2010**, *5*, 651.

[3] J. Lin, C. G. Zhang, Z. Yan, Y. Zhu, Z. W. Peng, R. H. Hauge, D. Natelson, J. M. Tour, *Nano Lett.* **2013**, *13*, 72.
[4] J. R. Miller, P. Simon, *Science* **2008**, *321*, 651.
[5] C. Z. Meng, J. M. Maeng, S. W. M. John, P. P. Irazoqui, *Adv. Energy Mater.* **2014**, *4*, 1301269.
[6] Z. S. Wu, K. Parvez, A. Winter, H. Vieker, X. J. Liu, S. Han, A. Turchanin, X. L. Feng, K. Müllen, *Adv. Mater.* 2014, 26, 4552.
[7] M. Mazloumi, S. Shadmehr, Y. Rangom, L. F. Nazar, X. W. (Shirley) Tang, *ACS Nano* **2013**, *7*, 4281.
[8] Z. Q. Niu, L. Zhang, L. L. Liu, B. W. Zhu, H. B. Dong, X. D. Chen, *Adv. Mater.* **2013**, *25*, 4035.
[9] Y. X. Xu, Z. Y. Lin, X. Q. Huang, Y. Liu, Y. Huang, X. F. Duan, *ACS Nano* **2013**, *7*, 4042.
[10] S. Ratha, C. S. Rout, *ACS Appl. Mater. Interfaces* **2013**, *5*, 11427.
[11] Z. S. Wu, K. Parvez, X. L. Feng, K. Müllen, *Nat. Commun.* **2013**, *4*, 2487.
[12] M. F. El-Kady, B. K. Richard, *Science* **2012**, *335*, 1326.
[13] V. Strong, S. Dubin, M. F. EI-Kady, A. Lech, Y. Wang, B. H. Weiller, R. B. Kaner, *ACS Nano* **2012**, *6*, 1395.
[14] M. F. El-Kady, V. Strong, S. Dubin, R. B. Kaner, *Nat. Commun.* **2013**, *4*, 1475.
[15] J. Feng, X. Sun, C. Wu, L. Peng, S. Hu, *J. Am. Chem. Soc.* **2011**, *133*, 17832.
[16] C. Z. Wu, X. L. Lu, L. L. Peng, K. Xu, X. Peng, J. L. Huang, G. H. Yu, Y. Xie, *Nat. Commun.* **2013**, *4*, 2431.
[17] X. F. Wang, B. Liu, Q. F. Wang, W. F. Song, X. J. Hou, D. Chen, Y. B. Cheng, G. Z. Shen, *Adv. Mater.* **2013**, *25*, 1479.
[18] S. Balendhran, S. Walia, H. Nili, J. Z. Ou, S. Zhuiykov, R. B. Kaner, S. Sriram, M. Bhaskaran, K. Kalantar-zadeh, *Adv. Funct. Mater.* **2013**, *23*, 3952.
[19] K. J. Koski, Y. Cui, *ACS Nano* **2013**, *7*, 3739.
[20] H. S. S. R. Matte, S. Gomathi, A. K. Manna, D. J. Late, R. Datta, S. K. Pati, C. N. R. Rao, *Angew. Chem. Int. Ed.* **2010**, *49*, 4059.
[21] L. J. Cao, S. B. Yang, W. Gao, Z. Liu, Y. J. Gong, L. L. Ma, G. Shi, S. D. Lei, Y. H. Zhang, S. T. Zhang, *Small* **2013**, *9*, 2905.
[22] Y. Fang, B. Luo, Y. Y. Jia, X. L. Li, B. Wang, Q. Song, F. Y. Kang, L. J. Zhi, *Adv Mater.* **2012**, *24*, 6348.
[23] M. Beidaghi, C. Wang, *Adv. Funct. Mater.* **2012**, *22*, 4501.
[24] W. P. Si, C. L. Yan, Y. Chen, S. Oswald, L. Y. Han, O. G. Schmidt, *Energy Environ. Sci.* **2013**, *6*, 3218.
[25] Y. He, Y. L. Zhong, F. Peng, X. P. Wei, Y. Y. Su, S. Su, W. Gu, L. S. Liao, S. T. Lee, *Angew. Chem. Int. Ed.* **2011**, *50*, 3080.
[26] Y. He, Y. L. Zhong, Y. Y. Su, Y. M. Lu, Z. Y. Jiang, F. Peng, T. T. Xu, S. Su, Q. Huang, C. H. Fan, S. T. Lee, *Angew. Chem. Int. Ed.* **2011**, *50*, 5695.
[27] P. A. Bertrand, *Phys. Rev. B* **1991**, *44*, 5745.
[28] H. Li, Q. Zhang, C. C. R. Yap, B. K. Tay, T. H. T. Edwin, A. Olivier, D. Baillargeat, *Adv. Funct. Mater.* **2012**, *22*, 1385.
[29] G. Plechinger, S. Heydrich, J. Eroms, D. Weiss, C. Schüller, T. Lorn, *Appl. Phys. Lett.* **2012**, *11*, 101906.
[30] B. J. Li, M. Ai, Z. Xu, *Chem. Commun.* **2010**, *46*, 6267.
[31] J. M. Soon, K. P. Loh, *Electrochem. Solid-State Lett.* **2007**, *10*, A250.
[32] B. L. Hu, X. Y. Qin, A. M. Asiri, K. A. Alamry, A. O. AI-Youbi, X. P. Sun, *Electrochim. Acta* **2013**, *100*, 24.
[33] M. Shahid, J. L. Liu, I. Shakir, M. F. Warsi, M. Nadeem, Y. U. Kwon, *Electrochim. Acta* **2012**, *85*, 243.
[34] G. F. Ma, H. Peng, J. J. Mu, H. H. Huang, X. Z. Zhou, Z. Q. Lei, *J. Power. Sources.* **2013**, *229*, 72.
[35] S. Vijayakumar, S. Nagamuthu, G. Muralidharan, *ACS Appl. Mater. Interfaces* **2013**, *5*, 2188.